



IR photothermal and spectroscopic analysis of proton-irradiated 4H-SiC

M. Hadi^a, J. Younes^a, M. Soueidan^b, M. Kazan^{a,*}

^a Department of Physics, American University of Beirut, P.O. Box 11-0236, Riad El-Solh, Beirut 1107-2020, Lebanon

^b Lebanese National Council for Scientific Research, Lebanese Atomic Energy Commission, P.O. Box 11-8281, Riad El Solh 1107, 2260 Beirut, Lebanon

ARTICLE INFO

Keywords:

Infrared photothermal effects
Infrared Spectroscopy
Subsurface defects

ABSTRACT

The effect of the proton irradiation dose on thermal transport anisotropy, free carrier density, and defect formation in 4H-SiC is studied by thermal wave scattering and infrared spectroscopy. Thermal waves are generated by infrared laser pulses, and the in-plane and cross-plane thermal diffusion length are measured using the deflection of a laser probe beam due to the mirage effect. The effect of proton irradiation dose on in-plane and cross-plane thermal diffusivity is measured as a function of depth. Proton irradiation is shown to cause significant damage primarily in the direction perpendicular to the sample surface. Irradiation-induced free carriers contributing to heat transport in the sample plane are revealed by Kramers-Kronig analysis of the infrared reflectivity spectra of the studied samples. Measurements of thermal diffusion lengths in the irradiated samples are converted to depth profiles of defect density. It is shown that the highly damaged zone in irradiated 4H-SiC thickens and approaches the proton reaching depth with increasing the irradiation dose. Thermal wave scattering complemented by infrared spectroscopy is proposed as an effective approach for the directional analysis of irradiation-induced changes in physical and structural properties of materials.

1. Introduction

Silicon carbide (SiC) crystallizes in many structures called polytypes. The 4H-SiC polytype, which consists of four atomic layers stacked in a hexagonal Bravais lattice, has received increased attention because it corresponds to a wide-bandgap semiconductor with electrical, mechanical, and thermal properties suitable for high-power devices operating in harsh environments [1–7], including nuclear reactors [8–10]. Extensive research has therefore been conducted on the effects of many types of nuclear irradiation on 4H-SiC [11–25]. Proton irradiation of 4H-SiC has been of particular interest since it was discovered that proton-slicing technology can provide ultra-thin single-crystalline 4H-SiC substrates [26–28].

Lattice damage due to proton irradiation of 4H-SiC has been experimentally detected [29–34], and it is now well known that a heavily damaged zone forms near the end of the proton trajectory. However, the extent to which proton irradiation changes the physical properties of 4H-SiC remains unclear. Revealing the properties of proton-irradiated 4H-SiC is certainly crucial for predicting the performance and lifetime of devices based on 4H-SiC material exposed to a given dose of proton irradiation. Common experimental techniques used to characterize proton-irradiated materials are secondary ion mass spectroscopy (SIMS),

Rutherford backscatter spectroscopy (RBS), and cross-sectional Raman spectroscopy. SIMS and RBS are accurate in measuring the depth profiles of ions concentrations in proton-irradiated samples [35]. Channeling RBS and cross-sectional Raman spectroscopy, on the other hand, have been widely used to provide a depth profile of the defect density in irradiated materials [30–32]. Nevertheless, none of these techniques can reveal the crystallographic directions along which defects form and measure the effect of proton irradiation on the anisotropy of the physical properties of the irradiated material.

In this paper, we address this issue and perform a directional analysis of thermal diffusivity and defect density depth profiles in 4H-SiC substrates irradiated with 3 MeV protons with different irradiation doses using thermal wave interaction with irradiation-induced defects. Thermal waves are generated by a modulated infrared (IR) pump laser beam, and the temperature gradient on the surface is detected using the deflection of a He-Ne probe beam due to the mirage effect. Then, photothermal spectrum analysis is performed based on a simple model to obtain the direction-dependent thermal transport properties and depth profiles of the defect density in the measured samples. The IR reflectivity spectra of the studied samples are analyzed using the Kramers-Kronig theorem to complement the IR photothermal measurements and obtain a complete picture of the effect of irradiation dose on the

* Corresponding author.

E-mail address: mk140@aub.edu.lb (M. Kazan).

<https://doi.org/10.1016/j.infrared.2021.103891>

Received 28 April 2021; Received in revised form 22 August 2021; Accepted 25 August 2021

Available online 28 August 2021

1350-4495/© 2021 Elsevier B.V. All rights reserved.

structural and electrical properties of 4H-SiC. The advantage of using an IR pump beam comes from the fact that 4H-SiC has a high absorption coefficient for IR excitations, allowing for the absorption of a significant amount of incident IR light in the surface layers, which is essential for locating the depths of the scattering centers. The advantage of IR spectroscopy, on the other hand, stems from the fact that defects in polar materials can be detected through their marked signatures in the IR spectrum and that the density of free carriers can be revealed through the coupling between plasmon modes and infrared-active longitudinal phonon modes. Therefore, the photothermal and IR spectroscopic techniques used in the present work are proposed to characterize the defects induced below the surface by irradiation and measure their effect on the material properties.

2. Methods

Five samples were cut from a commercial *n*-type *c*-oriented 4H-SiC wafer with electrical resistivity of 0.021 Ω.cm. Four were irradiated with 3 MeV protons (H⁺ ions) at doses of 2.5×10^{15} , 5.0×10^{15} , 1.0×10^{16} , and 2.0×10^{16} ions/cm², and one was left intact. The implantation of the H⁺ ions was performed at room temperature and the samples were tilted about 7° relative to the axis of the ion beam to avoid ion channeling effect. Conventional Monte Carlo simulations using the SRIM code [36] showed that the depth-concentration profiles of hydrogen in the irradiated samples exhibit a narrow peak centered at a depth of 60 ± 5 μm. Thus, as shown schematically in Fig. 1, each of the irradiated samples studied in this work consists of an irradiated layer of thickness $a_1 = 60 \pm 5$ μm separated from an intact 4H-SiC substrate by a zone of high H⁺ ion concentration.

The anisotropy of the thermal diffusion length in the samples was studied using an IR photothermal beam-deflection technique. The

schematic diagram describing the IR photothermal experiment used is shown in Fig. 1. An acousto-optic modulator modulates a 10.6 μm wavelength CO₂ laser focused on the sample surface. Absorption of the incident IR beam by the infrared-active phonon and plasmon modes causes periodic local heating and periodic displacement of the surface, as well as the generation of rapidly damped thermal waves in the air above the heated surface. An incident He-Ne laser probe beam with a grazing angle (0.5° from the sample surface) is reflected off the heated surface. The surface displacement only contributes to the longitudinal deflection (parallel to the heating beam) of the probe beam. The thermal waves generated in the air, on the other hand, give rise to periodic gradients of temperature and refractive index capable of periodically deflecting the probe beam parallel and perpendicular to the heating beam, at the modulation frequency of the infrared heating beam. The transverse deflection of the probe beam is thus due solely to the mirage effect. The angular deflection of the probe beam is recorded with a four-quadrant photodetector whose outputs are amplified with a two-channel lock-in amplifier. Readers can find more details about the experimental setup in Ref. [37,38]. Then, the in-plane and cross-plane thermal diffusion length in the measured sample are obtained as a function of the modulation frequency by fitting the measured transverse angular deflection of the probe beam to a formalism for the mirage effect assuming periodic and anisotropic heating of the sample. For the intact sample (a semi-infinite material), it is assumed that periodic heating generates a single forward-going thermal wave in the sample. In that case, the formalism for the transverse deflection of the probe beam can be written as

$$M_{trans} = \frac{-i}{\pi} \frac{1}{n} \frac{dn}{dT} e^{-q_g^2 R_2^2/4} \int_0^\infty dk \frac{k_g \sin(kx) e^{ik_s h} e^{-k^2 R_1^2/4}}{(\kappa_{1,z} k_1 + \kappa_g k_g)} \quad (1)$$

where x is the offset distance between the heating beam and probe beam. Here, n is the index of refraction of the air, R_1 is the radius of the pump beam, R_2 is the radius of the probe beam above the heated region, h is the height of the probe beam from the surface, $\kappa_{1,z}$ is the cross-plane thermal conductivity of the sample, and κ_g is the thermal conductivity of the air. The thermal wavevector in the sample is defined as

$$k_1 = \left(q_1^2 - \frac{L_{th}^2}{L_{th,z}^2} k^2 \right)^{1/2} \quad (2)$$

where L_{th} and $L_{th,z}$ are the in-plane and cross-plane thermal diffusion length. The thermal wavenumber q_1 depends on $L_{th,z}$ according to

$$q_1 = (1+i) \left(\frac{1}{L_{th,z}} \right) \quad (3)$$

The thermal wavevector in the air is given by $k_g = (q_g^2 - k^2)^{1/2}$,

where $q_g = (1+i)(\Omega/2\alpha_g)^{1/2}$, Ω is the heating beam modulation frequency, and α_g is the thermal diffusivity of the air. The derivation of Eq. (1) is detailed in Refs. [37,38] and in Supplementary Information 1. To reduce the number of adjustable parameters, R_2 is measured using the knife-edge method and R_1 is estimated from the photothermal beam-deflection theory, which predicts that the maximum of the transverse signal amplitude occurs at $r = 1.1 \times R_1$ [39]. Moreover, we can notice from Eqs. (2) and (3) that $L_{th,z}$ has almost the same effect on the real and imaginary part of the thermal wavevector k_1 . In other words, $L_{th,z}$ affects the propagation term and the damping term of the generated thermal wave in the same way and therefore has no significant influence on the amplitude and phase of the transverse signal. Consequently, for semi-infinite materials, the photothermal beam-deflection technique is insensitive to L_{th} and the only adjustable parameters are R_1 , h , and the in-plane thermal diffusion length L_{th} .

For a given modulation frequency Ω , the in-plane thermal diffusivity $\alpha_{//}$ is related to L_{th} by

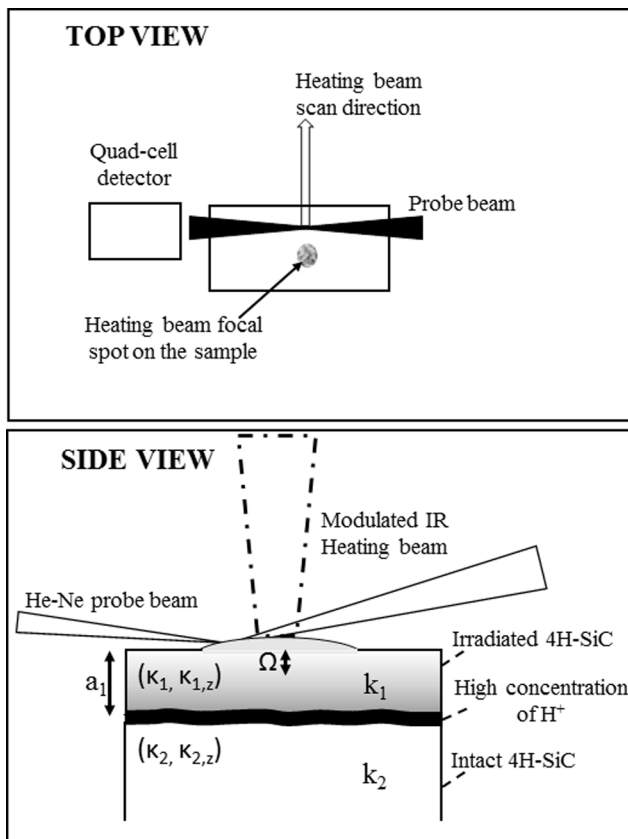


Fig. 1. Schematic representation of the proton-irradiated 4H-SiC samples investigated in this work and the infrared photothermal beam-deflection technique.

$$L_{th} = \sqrt{\frac{\alpha_l}{\pi\Omega}} \quad (4)$$

Thus, the in-plane thermal diffusivity of the intact sample can be obtained by measuring L_{th} for several modulation frequencies and calculating the slope of the straight line passing through origin that best fits the measured L_{th}^2 as a function of $1/\pi\Omega$.

As mentioned previously, the irradiated samples are considered to be formed by an irradiated layer with a thickness $a_1 = 60 \pm 5 \mu\text{m}$ separated from an intact 4H-SiC substrate by a zone of high hydrogen concentration. It is therefore assumed that in the case of irradiated samples, the thermal waves generated are backscattered at the interface between the irradiated and intact 4H-SiC. When forward-going and backward-going thermal waves are taken into account, the formalism for the transverse angular deflection of the probe beam takes the form

$$M_{trans} = \frac{-i}{\pi} \frac{1}{n} \frac{dn}{dT} e^{-q^2 R_2^2/4} \int_0^\infty dk \frac{k_g \sin(kx) e^{ik_g h} e^{-k^2 R_1^2/4}}{(\kappa_{1,z} k_1 \coth(\theta_1) + \kappa_g k_g)} \quad (5)$$

The complex constant θ_1 describing the relative amplitude and phase between the forward-going and the backward-going thermal waves in the irradiated region is given by

$$\theta_1 = -ik_1 a_1 + \text{atanh} \left(\frac{\kappa_{1,z} k_1}{\kappa_{2,z} k_2} \right) \quad (6)$$

Here, k_1 and k_2 are the thermal wavevectors in the irradiated and intact 4H-SiC, respectively. These wavevectors depend on the in-plane and the cross-plane thermal diffusion length, which in turn depend on the modulation frequency (see Eqs. (2) and (3)). The parameters $\kappa_{1,z}$ and $\kappa_{2,z}$ are the cross-plane thermal conductivities of the irradiated and intact 4H-SiC, respectively. The derivation of Eq. (5) is detailed in Ref. 40 and in [Supplementary Information 2](#). It is worth noting that the relative amplitude and phase between the forward-going and the backward-going thermal waves in the irradiated 4H-SiC makes the transverse angular deflection of the probe beam dependent on both the in-plane and cross-plane thermal diffusion length. Consequently, in the case of multilayer systems, the adjustable parameters are R_1 , h , as well as the in-plane thermal diffusion length L_{th} and the cross-plane thermal diffusion length $L_{th,z}$. The in-plane and cross-plane thermal diffusivity of the irradiated 4H-SiC can be obtained by following the procedure presented above for the case of a semi-infinite material.

To obtain information on the effect of irradiation dose on the structural and electrical properties of 4H-SiC, Fourier transform IR (FTIR) reflectivity measurements were performed on the samples described above. The measurements were carried out in the frequency range $400\text{--}4000 \text{ cm}^{-1}$ using a deuterated triglycine sulfate (DTGS) detector and a potassium bromide (KBr) beamsplitter. The IR beam was unpolarized and the angle of incidence was set at 45° to excite zone center optical phonon modes of different symmetries [41]. The reflectivity spectrum of each sample was normalized to the reflectivity spectrum of a gold mirror and the reproducibility of the measurements was checked by measuring the reflectivity spectra of the samples several times. The FTIR spectrometer has been carefully designed to ensure that the plane wave approximation is valid for the reflected IR beam to allow accurate Kramers-Kronig conversion of the reflectivity spectra. It is worth noting that the resonance of the phonon and plasmon modes in the IR spectral range makes the absorption coefficient of 4H-SiC very high for an IR excitation. In addition, irregularities at the hydrogen-enriched interface between irradiated 4H-SiC and intact 4H-SiC scatter infrared light and prevent interference between rays reflected from irradiated 4H-SiC and rays reflected from intact 4H-SiC. Therefore, the recorded IR reflectivity spectra are essentially dictated by the phonon and plasmon modes in the irradiated 4H-SiC, and their Kramers-Kronig conversions provide the real and imaginary parts of the infrared dielectric functions of the irradiated 4H-SiC layers only.

3. Results and discussion

3.1. Characterization of defects induced by proton irradiation

The amplitude and phase of the transverse signal from the intact sample are shown in [Fig. 2](#) as a function of the offset distance between the heating beam and probe beam and for nine different modulation frequencies. The amplitude increases as the heating beam moves closer to the probe beam, then goes sharply to zero when the two beams overlap. At this point, the phase shifts by 2π and the amplitude repeats itself as a mirror image. When the phase of the signal reaches -2π or $+2\pi$, it changes sign. Beyond an offset distance of a few thermal diffusion lengths, mechanical coupling to the direct heated regions of the sample dominates, causing the phase to fluctuate. This part of the recorded spectra was omitted from consideration in the data analysis. The in-plane thermal diffusion length in the intact sample is obtained for each modulation frequency by simultaneously fitting the amplitudes and phases of the transverse signals to Eq. (1). The high quality of the multi-parameter least squares fits of the amplitudes and phases of the transverse signals from the intact sample is illustrated in [Fig. 2](#). The in-plane thermal diffusivity L_{th} of that sample is obtained, as shown in [Fig. 3](#), from the slope of the straight line passing through origin that best fits the measured L_{th}^2 vs. $1/\pi\Omega$. An in-plane thermal diffusivity of $2.00 \pm 0.04 \text{ cm}^2/\text{s}$ is obtained for intact 4H-SiC. This value corresponds to an in-plane thermal conductivity of 443 W/m.K , which is in agreement with results of thermal measurements and first-principles calculations on 4H-

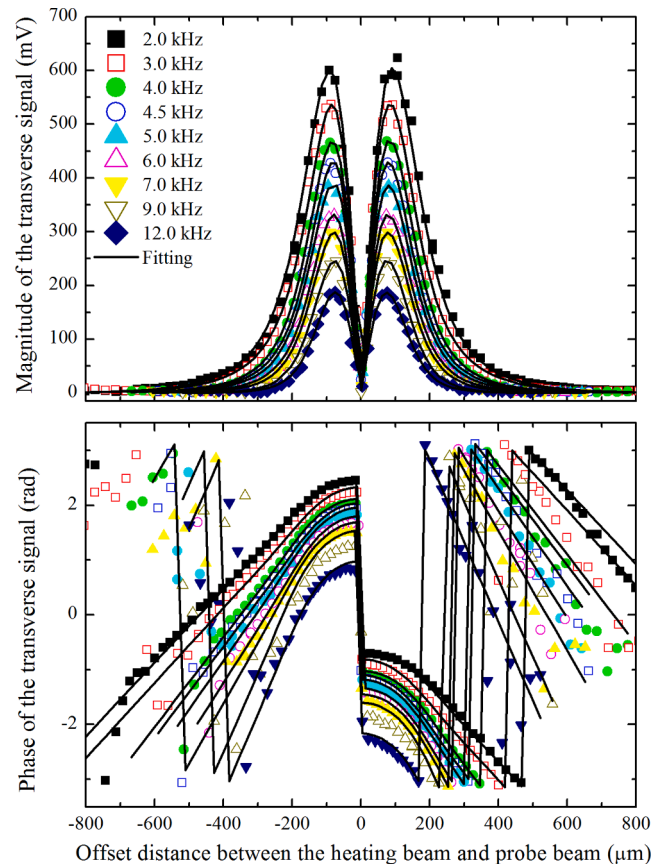


Fig. 2. Magnitude and phase of the transverse photothermal signal from an intact 4H-SiC substrate as a function of the offset distance between the heating beam and probe beam for nine different heating beam modulation frequencies. The symbols represent the experimental data. The solid lines represent the fits of the experimental data to a formalism for the angular deflection of the probe beam due to the mirage effect with taking into account a single forward-going thermal wave.

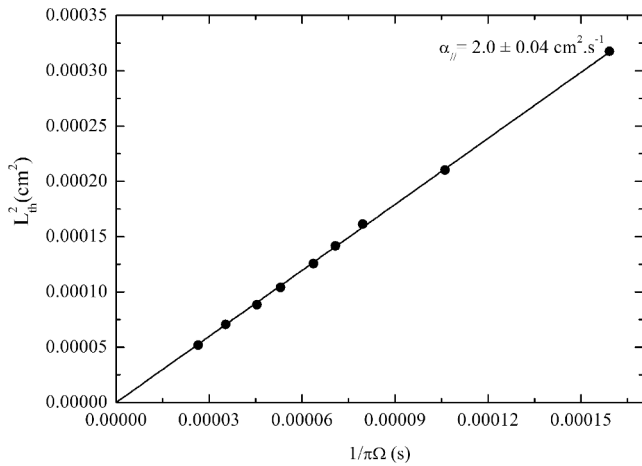


Fig. 3. Square of in-plane thermal diffusion length in intact 4H-SiC substrate vs. $1/\pi\Omega$, where Ω is the heating beam modulation frequency. The data set is fitted to a straight line passing through origin whose slope is equal to the in-plane thermal diffusivity of the measured sample. The uncertainties are determined by the experiment sensitivity and the scatter in the data points.

SiC reported previously [42,43].

The amplitudes and phases of the transverse signals from the proton-irradiated 4H-SiC samples are presented in [Supplementary Information 3](#) as a function of the offset distance between the heating beam and probe beam and for nine different modulation frequencies. An excellent description of the experimental data is obtained by fitting the measured transverse signals to Eq. (5), which accounts for thermal waves backscatter at the hydrogen-enriched zone near the proton reaching depth.

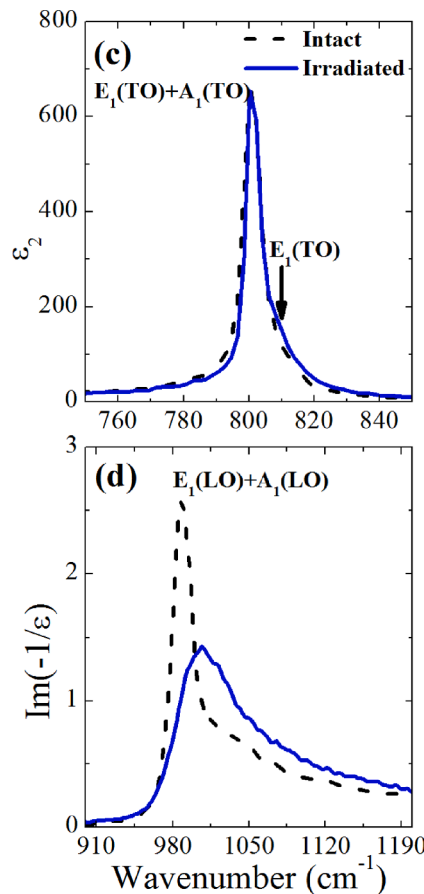
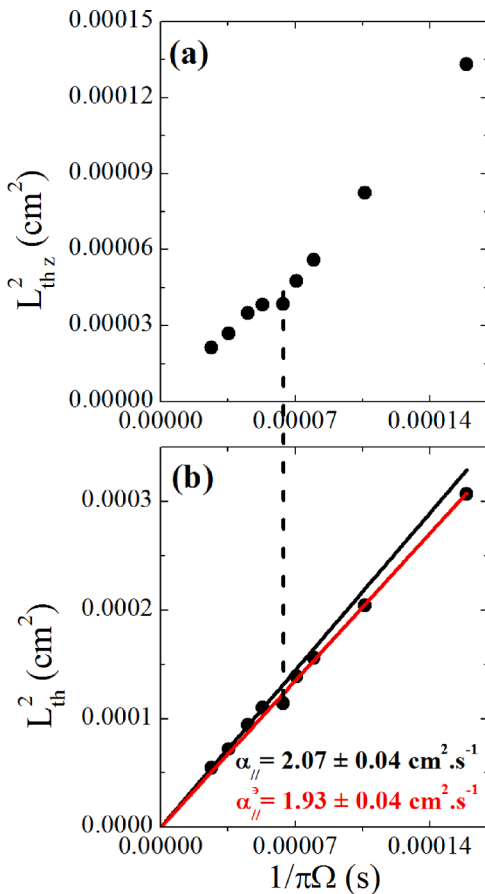


Fig. 4. Infrared analysis of 4H-SiC substrate irradiated with protons at 3 MeV with a dose of 2.5×10^{15} H^+ ions/cm². (a) Square of cross-plane thermal diffusion length $L_{th,z}^2$ vs. the inverse of π times the heating beam modulation frequency. (b) Square of in-plane thermal diffusion length L_{th}^2 vs. the inverse of π times the heating beam modulation frequency. The slopes of the straight line passing through origin that best fit the data points give the in-plane thermal diffusivity for high and low heating beam modulation frequencies. The uncertainties are determined by the experiment sensitivity and the scatter in the data points. The vertical dashed line is introduced to highlight the fact that $L_{th,z}^2$ and L_{th}^2 undergo the strongest deviation from the linear behavior for the same modulation frequency. (c) Imaginary parts of the infrared dielectric functions of intact 4H-SiC and the irradiated sample. (d) Imaginary parts of the inverse of the negative of the dielectric functions of intact 4H-SiC and the irradiated sample.

As demonstrated in [Section 2](#), thermal waves backscattering at the interface between irradiated and intact 4H-SiC allows measurement of both the in-plane and cross-plane thermal diffusion length. The results obtained from the best fit of the measured transverse signals from the irradiated samples to Eq. (5) are presented below.

The cross-plane thermal diffusion length $L_{th,z}$ in the 4H-SiC layer irradiated with a proton dose of 2.5×10^{15} ions/cm² is plotted in [Fig. 4](#) (a) as a function of $1/\pi\Omega$. For high modulation frequencies (i.e., when the thermal wave dies out before reaching the irradiation-induced highly damaged zone), the measured $L_{th,z}$ is shorter than the cross-plane thermal diffusion length of defect-free 4H-SiC (as can be concluded from Refs. 42 and 43), indicating irradiation-induced defects along the axis of the hexagonal unit cell of the irradiated 4H-SiC. For moderate modulation frequencies, the thermal wave scatters at the highly damaged zone in the irradiated 4H-SiC layer and $L_{th,z}$ shortens further to the order of the irradiated layer. At this point, $L_{th,z}^2$ deviates strongly from the linear dependence on $1/\pi\Omega$. For low modulation frequencies, the thermal wavelength becomes significantly larger than the thickness of the irradiated 4H-SiC layer, and thus the rate at which thermal waves are scattered by the irradiation-induced defects decreases with the modulation frequency. Therefore, $L_{th,z}^2$ increases again with $1/\pi\Omega$.

The in-plane thermal diffusion length L_{th} in the 4H-SiC layer irradiated with a proton dose of 2.5×10^{15} ions/cm² is plotted in [Fig. 4](#)(b) as a function of $1/\pi\Omega$. For high modulation frequencies, L_{th} is comparable to and even slightly longer than the in-plane thermal diffusion length of the intact sample, indicating that proton irradiation with a dose of 2.5×10^{15} ions/cm² does not cause any noticeable damage in the basal plane of the 4H-SiC hexagonal unit cell. The origin of the slight increase in L_{th} observed in the irradiated 4H-SiC will be discussed later. For lower modulation frequencies, the penetration depth increases and the

measured in-plane thermal wave propagates in a layer including the highly damaged zone that occurs near the end of the proton trajectory. Because the thermal diffusivity of the highly damaged zone is significantly low [44–48], the overall in-plane thermal diffusivity decreases, and consequently, the measured L_{th}^2 deviates from the linear dependence on $1/\pi\Omega$. The relationship between the in-plane thermal diffusivity of the highly damaged zone and the overall in-plane thermal diffusivity of the measured 4H-SiC layer is provided in [Supplementary Information 4](#).

To complement the photothermal measurements, FTIR reflectivity measurements were performed on the intact and irradiated samples. The FTIR reflectivity spectra from the samples investigated in this work are shown together in [Supplementary Information 5](#). The frequency-dependent infrared complex dielectric functions $\epsilon(\omega)$ of the samples were obtained from the Kramers-Kronig (KK) conversion of the measured FTIR reflectivity spectra. The KK theorem was implemented with necessary precautions to minimize the error that can result from integration over a finite frequency range [49]. The resonances of the TO phonon modes are obtained from the imaginary part of the dielectric function and the resonances of the LO phonon modes are obtained from the imaginary part of the negative of the inverse of the dielectric function. The plasmon modes (i.e., the vibration modes corresponding to collective oscillations of free carriers) are also infrared-active and should show signatures in the IR spectrum. However, the frequencies of the LO phonon and plasmon modes usually occur very close to each other, and therefore, they couple through their associated electric fields to give rise to the so-called longitudinal plasmon-phonon mode [50–53]. The plasmon-phonon coupling manifests itself by a resonance frequency higher than that of the LO phonon mode and by a broad and asymmetric resonance line in the IR spectrum.

The resonance lines of the infrared-active transverse optical (TO) phonons in the intact sample and the sample irradiated with a dose of

2.5×10^{15} ions/cm² are shown in [Fig. 4\(c\)](#), and the resonance lines of the infrared-active longitudinal optical (LO) phonons in these samples are shown in [Fig. 4\(d\)](#). The detected phonons are of pure E_1 symmetry and A_1 - E_1 mixed-symmetry. The identification of the symmetries of the infrared-active phonons in 4H-SiC is provided in [Supplementary Information 6](#). No noticeable effect of proton irradiation at a dose of 2.5×10^{15} ions/cm² is observed on the imaginary part of the infrared dielectric function. This result indicates that the lattice damage density induced by proton irradiation at a dose of 2.5×10^{15} ions/cm² is high enough to scatter cross-plane thermal waves, but low enough not to be observed by vibrational spectroscopy.

As the substrate used in this work is *n*-type, the resonance line of the LO phonon in the intact sample exhibits an asymmetric peak with a broad tail at high frequencies, indicating coupling between the A_1 - E_1 mixed-symmetry LO phonon mode with a plasmon mode. The resonance line of the LO phonon in the sample irradiated with a proton dose of 2.5×10^{15} ions/cm², however, is shifted towards higher frequencies and is broader, indicating irradiation-induced additional free carriers in the proton-irradiated layer. As shown above, proton irradiation of 4H-SiC with a dose of 2.5×10^{15} ions/cm² causes no noticeable damage in the basal plane of the 4H-SiC hexagonal unit cell. Hence, the additional free carriers generated by proton irradiation can contribute to the in-plane heat transport in the sample and raise the in-plane thermal diffusivity of the irradiated layer over that of the intact sample, which accounts for the fact that the in-plane thermal diffusion length in the irradiated layer is slightly longer than that in the intact sample. Signature from the E_1 symmetry LO phonon is not observed because the plasmon-phonon mode resonance line overwhelms it.

The cross-plane and in-plane thermal diffusion length in the sample irradiated with a proton dose of 5.0×10^{15} ions/cm² are shown in [Fig. 5](#) (a) and (b), respectively, for nine different modulation frequencies. The

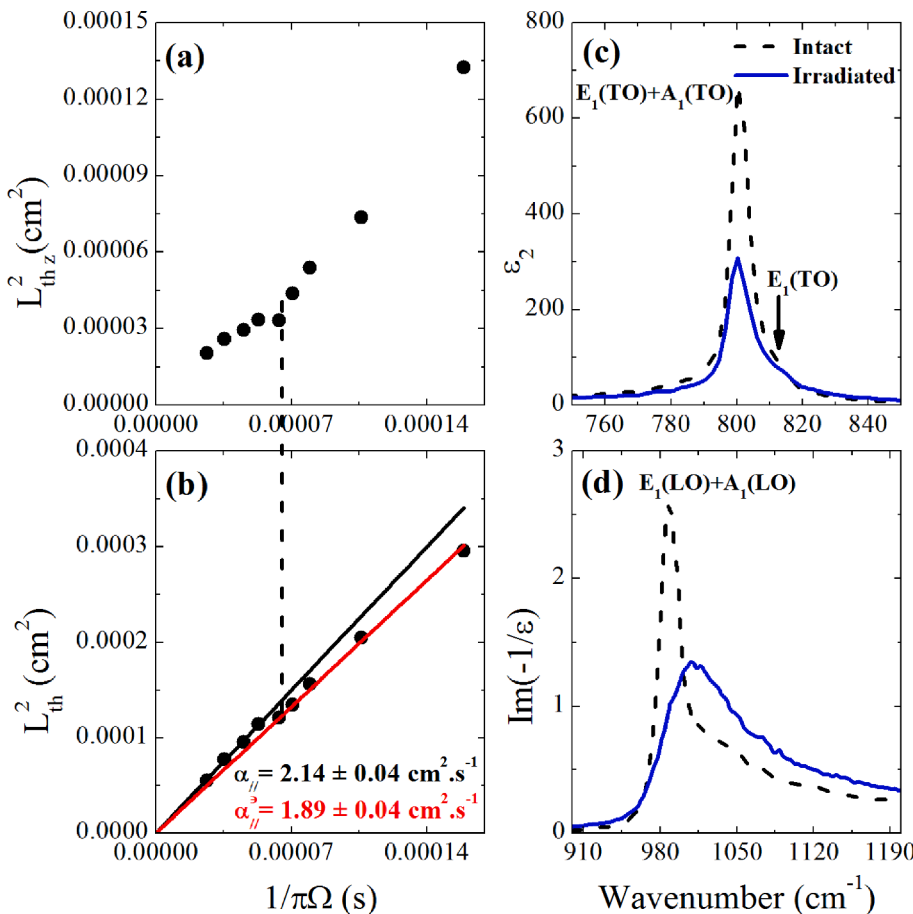


Fig. 5. Infrared analysis of 4H-SiC substrate irradiated with protons at 3 MeV with a dose of 5.0×10^{15} H⁺ ions/cm². (a) Square of cross-plane thermal diffusion length $L_{th,z}^2$ vs. the inverse of π times the heating beam modulation frequency. (b) Square of in-plane thermal diffusion length L_{th}^2 vs. the inverse of π times the heating beam modulation frequency. The slopes of the straight line passing through origin that best fit the data points give the in-plane thermal diffusivity for high and low heating beam modulation frequencies. The uncertainties are determined by the experiment sensitivity and the scatter in the data points. The vertical dashed line is introduced to highlight the fact that $L_{th,z}^2$ and L_{th}^2 undergo the strongest deviation from the linear behavior for the same modulation frequency. (c) Imaginary parts of the infrared dielectric functions of intact 4H-SiC and the irradiated sample. (d) Imaginary parts of the inverse of the negative of the dielectric functions of intact 4H-SiC and the irradiated sample.

curves describing the variation of the cross-plane thermal diffusion length $L_{th,z}$ and the in-plane thermal diffusion length L_{th} with $1/\pi\Omega$ are similar to those for the samples irradiated with a proton dose of 2.5×10^{15} ions/cm² except for two aspects. First, for all measured modulation frequencies, $L_{th,z}$ is shorter, indicating that the increase in proton irradiation dose causes a higher density of defect along the axis of the 4H-SiC unit cell. Second, the deviation of $L_{th,z}^2$ and L_{th}^2 from the linear dependence on $1/\pi\Omega$ is more pronounced, indicating that the highly damaged zone occurring near the end of the proton trajectory thickens with increasing the proton irradiation dose.

The infrared active TO and LO phonon resonances in the intact sample and the sample irradiated with a dose of 5.0×10^{15} ions/cm² are shown in Fig. 5(c) and (d) respectively. As can be seen in Fig. 5(c), the intensity of the TO phonon resonance line in the irradiated layer is lower than the intensity of the TO phonon resonance line in the intact 4H-SiC, indicating that for a proton irradiation dose of 5.0×10^{15} ions/cm², the lattice damage reaches a level detectable by vibrational spectroscopy. The comparison between the LO phonon resonance lines in the irradiated layer and in the intact 4H-SiC, shown in Fig. 5(d), clearly demonstrates that a proton irradiation dose of 5.0×10^{15} ions/cm² generates additional free carriers whose collective vibrational mode couples with the LO phonon mode. These irradiation-induced free carriers contribute to in-plane heat transport and slightly increase the in-plane thermal diffusivity of the irradiated layer over that of the intact sample.

The cross-plane and in-plane thermal diffusion length in the sample irradiated with a proton dose of 1.0×10^{16} ions/cm² are shown in Fig. 6 (a) and (b), respectively, for nine different modulation frequencies. For this irradiation dose, the curve of $L_{th,z}^2$ vs. $1/\pi\Omega$ gradually deviates from a straight line as the modulation frequency decreases. Then, it decreases sharply for modulation frequencies for which $L_{th,z}$ is of the order of the

thickness of the irradiated layer, and increases again for frequencies for which $L_{th,z}$ is significantly longer than the thickness of the irradiated layer. However, the rate at which this curve increases at low frequencies is markedly lower than the rate at which it increases for lower irradiation doses. This behavior of the $L_{th,z}^2$ vs. $1/\pi\Omega$ curve indicates that the highly damaged zone in the layer irradiated with a proton dose of 1.0×10^{16} ions/cm² is significantly thicker than that in the layers irradiated at lower doses. The curve describing the variation of the square of the in-plane thermal diffusion length L_{th}^2 with $1/\pi\Omega$ shown in Fig. 6(b) demonstrates, on the other hand, that even at such a high irradiation dose, proton irradiation does not cause any noticeable damage in the basal plane of the 4H-SiC unit cell. The fact that the deviation of L_{th}^2 from the linear dependence on $1/\pi\Omega$ when the thermal wave reaches the highly damaged region is now more pronounced than that observed in the cases of lower irradiation doses indicates that the highly damaged zone in the layer irradiated at a dose of 1.0×10^{16} ions/cm² is thicker than that in the layers irradiated at lower doses (see Supplementary Information 4).

The resonance lines of the infrared-active TO and LO phonons in the intact sample and the sample irradiated with a dose of 1.0×10^{16} ions/cm² are shown in Fig. 6(c) and (d), respectively. As shown in Fig. 6(c), at an irradiation dose of 1.0×10^{16} ions/cm², the A₁-E₁ mixed-symmetry TO phonon mode splits into two different modes. This phonon mode splitting is due to the effect of the high defect concentration in the highly damaged zone, which causes a stress field on the TO phonon resonance frequency [54,55]. Thus, at an irradiation dose of 1.0×10^{16} ions/cm², the highly damaged zone becomes thick enough to be detected in IR spectroscopy. The comparison between the resonance lines of the LO phonon modes in the irradiated layer and the intact 4H-SiC substrate demonstrates, as for the layers irradiated at lower doses, irradiation-induced additional free carriers whose collective vibrational mode

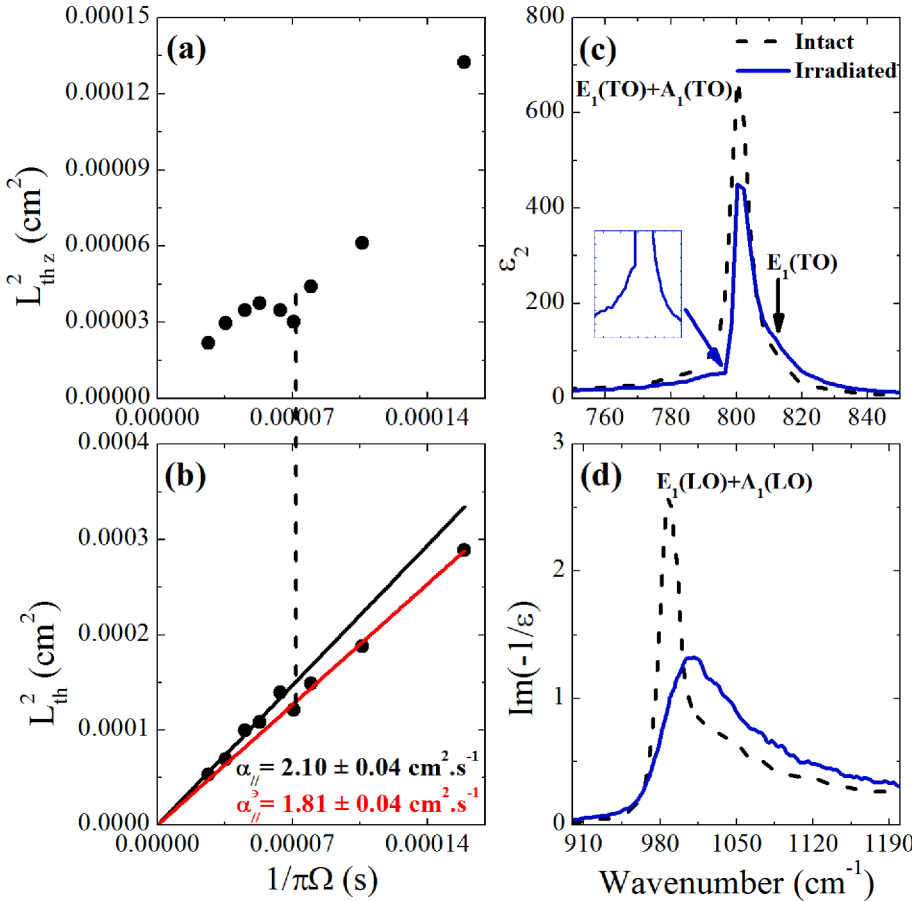


Fig. 6. Infrared analysis of 4H-SiC substrate irradiated with protons at 3 MeV with a dose of 1.0×10^{16} H⁺ ions/cm². (a) Square of cross-plane thermal diffusion length $L_{th,z}^2$ vs. the inverse of π times the heating beam modulation frequency. (b) Square of in-plane thermal diffusion length L_{th}^2 vs. the inverse of π times the heating beam modulation frequency. The slopes of the straight line passing through origin that best fit the data points give the in-plane thermal diffusivity for high and low heating beam modulation frequencies. The uncertainties are determined by the experiment sensitivity and the scatter in the data points. The vertical dashed line is introduced to highlight the fact that $L_{th,z}^2$ and L_{th}^2 undergo the strongest deviation from the linear behavior for the same modulation frequency. (c) Imaginary parts of the infrared dielectric functions of intact 4H-SiC and the irradiated sample. (d) Imaginary parts of the inverse of the negative of the dielectric functions of intact 4H-SiC and the irradiated sample.

couples with the LO phonon mode.

The cross-plane and in-plane thermal diffusion length in the sample irradiated with a proton dose of 2.0×10^{16} ions/cm² are shown in Fig. 7 (a) and (b), respectively, for nine different modulation frequencies. The very pronounced drop of $L_{th,z}^2$ and L_{th}^2 when the thermal wave approaches the highly damaged region indicate that when the proton irradiation dose increases to 2.0×10^{16} ions/cm², the thickness of the highly damaged zone increases further. The values of the in-plane thermal diffusion lengths for high modulation frequencies are very comparable to those of the intact 4H-SiC, indicating that even an extremely high irradiation dose (about one fifth of the dose at which 4H-SiC flakes are exfoliated [26]) does not cause any noticeable damage in the basal plane of the 4H-SiC unit cell.

The resonance lines of the infrared-active TO and LO phonons in the intact sample and the sample irradiated with a dose of 2.0×10^{16} ions/cm² are shown in Fig. 7(c) and (d), respectively. As the irradiation dose increases to 2.0×10^{16} ions/cm², the splitting of the A₁-E₁ mixed-symmetry TO phonon mode becomes more pronounced, indicating a further increase in the thickness of the highly damaged zone. The resonance line of the LO phonon, on the other hand, continues to reveal irradiation-induced free carriers.

3.2. Effect of proton irradiation dose on thermal diffusivity

The cross-plane and in-plane thermal diffusivity of the proton-irradiated layers can be obtained from the relation $L_{th,(z)}^2 \times \pi\Omega$, which corresponds to the slope of the tangent to the curve of $L_{th,(z)}^2$ vs. $1/\pi\Omega$. The thermal diffusion length measurements described above demonstrate that the cross-plane thermal diffusivity α_{\perp} gradually decreases with decreasing modulation frequency, and increases again when the mod-

ulation frequency falls below a critical frequency, and the rate at which α_{\perp} varies depends on the proton irradiation dose. The reason for this dependence of α_{\perp} on the modulation frequency and the proton irradiation dose is that, as shown above, proton irradiation induces defects along the axis of the 4H-SiC unit cell and a heavily damaged zone near the end of the proton trajectory, and the density of the induced defects and the thickness of the heavily damaged zone depend on the proton irradiation dose.

The in-plane thermal diffusivity α_{\parallel} is almost unaffected by proton irradiation for high modulation frequencies for which the in-plane thermal wave does not interact with the highly damaged zone, which occurs near the end of the proton trajectory. Nevertheless, when the modulation frequency falls below the critical frequency, the in-plane thermal wave interacts with the highly damaged zone, which is characterized by low thermal diffusivity, and consequently α_{\parallel} drops. As the thickness of the highly damaged zone depends on the proton irradiation dose, the drop of α_{\parallel} depends on the proton irradiation dose. The in-plane thermal diffusivity α_{\parallel} of 4H-SiC is presented in Table 1. as a function of the proton irradiation dose and for modulation frequencies

Table 1

In-plane thermal diffusivity α_{\parallel} of 4H-SiC as a function of the proton irradiation dose and for modulation frequencies above and below the critical frequency Ω_c .

Proton irradiation dose (ions/cm ²)	α_{\parallel} for $\Omega > \Omega_c$ (cm ² .s ⁻¹)	α_{\parallel} for $\Omega < \Omega_c$ (cm ² .s ⁻¹)
0	2.00 ± 0.04	2.00 ± 0.04
2.5×10^{15}	2.07 ± 0.04	1.93 ± 0.04
5.0×10^{15}	2.14 ± 0.04	1.89 ± 0.04
1.0×10^{16}	2.10 ± 0.04	1.81 ± 0.04
2.0×10^{16}	1.93 ± 0.04	1.49 ± 0.04

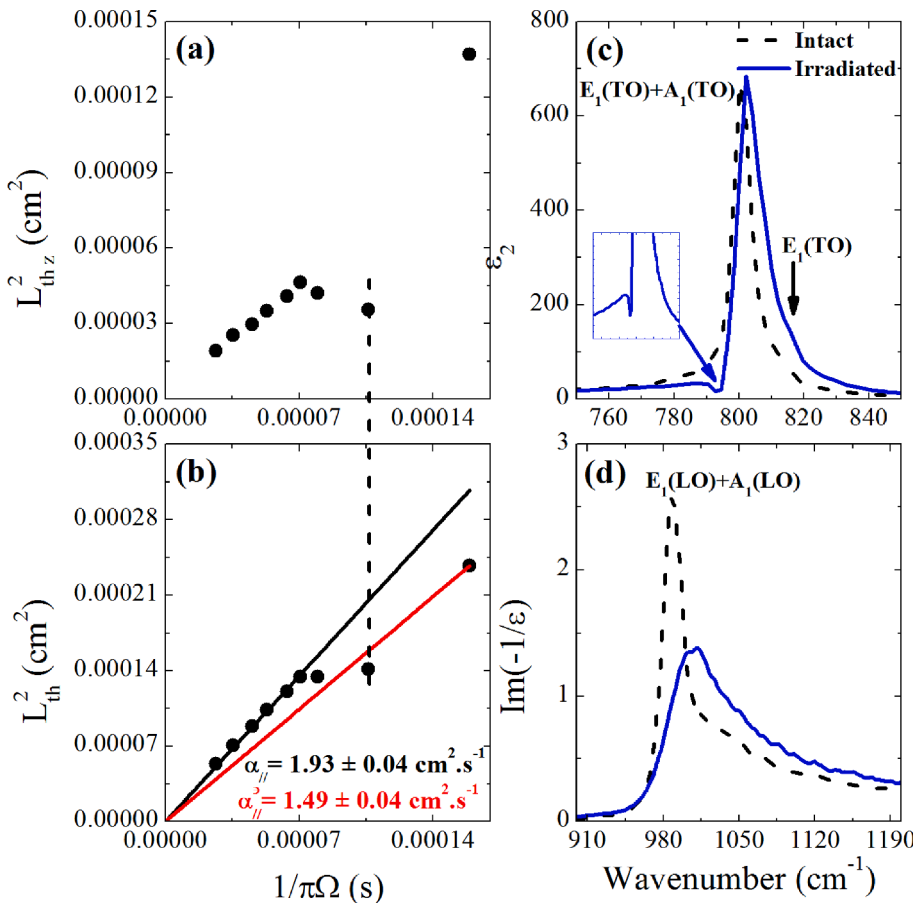


Fig. 7. Infrared analysis of 4H-SiC substrate irradiated with protons at 3 MeV with a dose of 2.0×10^{16} H⁺ ions/cm². (a) Square of cross-plane thermal diffusion length $L_{th,z}^2$ vs. the inverse of π times the heating beam modulation frequency. (b) Square of in-plane thermal diffusion length L_{th}^2 vs. the inverse of π times the heating beam modulation frequency. The slopes of the straight line passing through origin that best fit the data points give the in-plane thermal diffusivity for high and low heating beam modulation frequencies. The uncertainties are determined by the experiment sensitivity and the scatter in the data points. The vertical dashed line is introduced to highlight the fact that $L_{th,z}^2$ and L_{th}^2 undergo the strongest deviation from the linear behavior for the same modulation frequency. (c) Imaginary parts of the infrared dielectric functions of intact 4H-SiC and the irradiated sample. (d) Imaginary parts of the inverse of the negative of the dielectric functions of intact 4H-SiC and the irradiated sample.

above and below the critical frequency.

3.3. Effect of proton irradiation dose on the depth profile of axial defect density

The absorption of IR light in the surface layers of measured samples and the deviation of $L_{th,z}^2$ from the linear dependence on $1/\pi\Omega$ as the modulation frequency approaches the critical frequency Ω_c , which is indicated in Figs. 4(a-b), 5(a-b), 6(a-b), and 7(a-b) by dashed lines, provide an important tool for examining the distribution of irradiation-induced defect along the axis of the unit cell. The procedure for converting the measured curve of $L_{th,z}^2$ vs. $1/\pi\Omega$ into depth profile of axial defect density is presented in what follows. Let z be the depth of a scattering center (point defect, dislocation, impurity, etc...). Due to the high damping of the thermal wave generated on the surface by the IR heating beam, it is reasonable to assume that the characteristic thermal wavelength λ_z is equal to the cross-plane thermal diffusion length [40]. The sensitivity of the thermal wave to the scattering center at depth z increases as λ_z increases. For instance, if $\lambda_z \leq z$, the thermal wave is insensitive to the defect as it vanishes before reaching depth z , and if λ_z is slightly larger than z , the thermal wave hardly interacts with the defect at depth z . However, if $\lambda_z > 2z$, the thermal wave does not scatter at depth z because of the diffraction limit. Consequently, the most sensitive thermal wave to the scattering center at depth z is the one whose wavelength is equal to $2z$. On the other hand, the strength of the thermal wave scattering can be determined from the relative difference between the cross-plane thermal diffusion length in the measured layer and intact 4H-SiC ($\Delta L_{th,z}/L_{th,z}$). Here, $L_{th,z}$ is the cross-plane thermal diffusion length in intact 4H-SiC and $\Delta L_{th,z}$ is the absolute difference between the cross-plane thermal diffusion length in the measured layer and intact 4H-SiC. Thus, the plot of $\Delta L_{th,z}/L_{th,z}$ vs. $L_{th,z}/2$ (which, as mentioned above, is equal to $\lambda_z/2$) provides a measure of the strength of thermal wave scattering as a function of the scattering center depth in the measured layer. In other words, such a plot provides a depth profile of the axial defect distribution in the measured layer.

The plots of $\Delta L_{th,z}/L_{th,z}$ vs. $L_{th,z}/2$ for the irradiated 4H-SiC layers are presented in Fig. 8. These plots show that for low proton irradiation doses, the highly damaged zone is at approximately 12 μm from the hydrogen-enriched interface between the irradiated and intact 4H-SiC. However, as the proton irradiation dose increases, the heavily damaged zone approaches the hydrogen-enriched interface, which is located at a depth of $60 \pm 5 \mu\text{m}$. The plots illustrated in Fig. 8 also show that, in accordance with the conclusion drawn from the behavior of $L_{th,z}^2$ in the irradiated 4H-SiC layers, the thickness of the highly damaged zone increases as the proton irradiation dose increases.

4. Conclusion

Directional analysis of thermal diffusivity and defect density depth profiles in proton-irradiated 4H-SiC substrates is performed using an IR photothermal beam-deflection technique and IR spectroscopy. Pulses from a 10.6 μm wavelength CO_2 laser were used to generate thermal waves in 4H-SiC single crystal substrates irradiated with protons at 3 MeV with different irradiation doses. The induced temperature gradients on the surfaces were measured using the deflection of a He-Ne laser probe beam due to the mirage effect. The cross-plane and in-plane thermal diffusion lengths in the irradiated layers were obtained by fitting the measured angular deflection of the probe beam to a model for the mirage effect taking into account the anisotropic thermal properties of 4H-SiC. The variation of the square of the cross-plane thermal diffusion length relative to the inverse of the modulation frequency showed that proton irradiation causes significant damage along the axis of the hexagonal unit cell of 4H-SiC and that the highly damaged zone at which thermal waves scatter the most thickens as the irradiation dose increases. On the other hand, the variation of the square of the in-plane

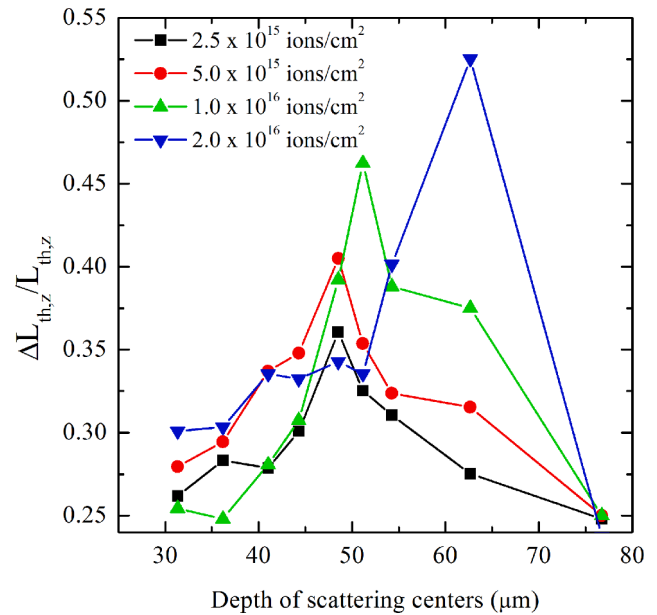


Fig. 8. Plots of the relative differences between the cross-plane thermal diffusion lengths in the irradiated 4H-SiC layers investigated in this work and in intact 4H-SiC vs. the half of the cross-plane thermal diffusion length in intact 4H-SiC revealing the depth profiles of the defect density in 4H-SiC substrates irradiated with protons at 3 MeV with different irradiation doses.

thermal diffusion length relative to the inverse of the modulation frequency showed that proton irradiation does not cause any noticeable damage in the basal plane of the 4H-SiC hexagonal unit cell. The effect of the proton irradiation dose on the cross-plane and in-plane thermal diffusivity of 4H-SiC was also deduced. The Kramers-Kronig conversion of the FTIR reflectivity spectra of the samples further confirmed that the thickness of the heavily damaged zone increases with the irradiation dose and showed that proton irradiation induces free carriers that can contribute to heat transport in the plane of the irradiated layer. The measurement of thermal wave scattering in the irradiated layers was used to generate the depth profile of the defect density in proton-irradiated 4H-SiC for different proton irradiation doses. The results showed that the highly damaged zone thickens and approaches the proton reaching depth as the irradiation dose increases. IR photothermal deflection and IR spectroscopy are proposed as effective tools to characterize deep subsurface defects and their effects on material properties.

Declaration of Competing Interest

The authors declare that they have no known competing financial interests or personal relationships that could have appeared to influence the work reported in this paper.

Acknowledgments

The authors gratefully acknowledge the financial support by Munib and Angela Masri Institute of Energy and Natural Resources, and the American University of Beirut Research Board (URB).

Appendix A. Supplementary material

Supplementary data to this article can be found online at <https://doi.org/10.1016/j.infrared.2021.103891>.

References

- [1] Y. Goldberg, M.E. Levinshstein, S.L. Rumvantsev, Properties of Advanced Semiconductor Materials GaN, AlN, SiC, BN, SiC, SiGe, in: M.E. Levinshstein, S.L. Rumvantsev, M.S. Shur, John Wiley & Sons, Inc., New York, 2001, pp. 93–148.
- [2] J.N. Shenoy, J.A. Cooper, M.R. Melloch, *IEEE Electron Device Lett.* 18 (3) (1997) 93.
- [3] T. Tadao, H. Masayuki, N. Yasuhiko, U. Yasuhiro, S. Minoru, S. Masayuki, *Jpn. J. Appl. Phys., Part 2* 43 (1A) (2004) L27.
- [4] R. Madar, *Nature* 430 (2004) 974.
- [5] T.H. Lee, S. Bhunia, M. Mehregany, *Science* 329 (2010) 1316.
- [6] C.R. Eddy, D.K. Gaskill, *Science* 324 (2009) 1398.
- [7] D. Nakamura, I. Gunjishima, S. Yamaguchi, T. Ito, A. Okamoto, H. Kondo, S. Onda, K. Takatori, *Nature* 430 (2004) 1009.
- [8] L.L. Snead, T. Nozawa, Y. Katoh, T.-S. Byun, S. Kondo, D.A. Petti, *J. Nucl. Mater.* 371 (2007) 329.
- [9] T. Koyanagi, Y. Katoh, T. Nozawa, *J. Nucl. Mater.* 540 (2020), 152375.
- [10] Y. Katoh, L.L. Snead, *J. Nucl. Mater.* 526 (2019), 151849.
- [11] A. Chakravorty, B. Singh, H. Jatav, S. Ojha, J. Singh, D. Kanjilal, D. Kabiraj, *J. Appl. Phys.* 128 (2020), 165901.
- [12] L. Nucklos, M.L. Crespillo, C. Xu, E. Zarkadoulas, Y.W. Zhang, W.J. Weber, *Acta Mater.* 199 (2020) 96.
- [13] X. Wang, H.L. Zhang, T. Baba, H. Jiang, C. Liu, Y.X. Guan, O. Elleuch, T. Kuech, D. Morgan, J.C. Idrobo, P.M. Voyles, I. Szlufarska, *Nat. Mater.* 19 (2020) 992.
- [14] L.B.B. Aji, J.B. Wallace, S.O. Kucheyev, *J. Appl. Phys.* 125 (2019), 235706.
- [15] L.L. Snead, Y. Katoh, T. Koyanagi, K. Terrani, *J. Nucl. Mater.* 514 (2019) 181.
- [16] L.B.B. Aji, E. Stavrou, J.B. Wallace, A. Boule, A. Debelle, S.O. Kucheyev, *Appl. Phys. A-Mater. Sci. Process.* 125 (2019) 28.
- [17] L.B.B. Aji, J.B. Wallace, S.O. Kucheyev, *Nucl. Instrum. Methods Phys. Res. Sect. B-Beam Interact. Mater. Atoms* 435 (2018) 8.
- [18] T. Koyanagi, Y. Katoh, M.J. Lance, *J. Raman Spectrosc.* 49 (2018) 1686.
- [19] X.F. Chen, W. Zhou, X.X. Zhang, Q.J. Feng, J. Zheng, X.K. Liu, B. Tang, J.B. Li, J. M. Xue, S.M. Peng, *J. Appl. Phys.* 123 (2018), 025104.
- [20] A. Boule, A. Debelle, J.B. Wallace, L.B.B. Aji, S.O. Kucheyev, *Acta Mater.* 140 (2017) 250.
- [21] X.X. Hu, T. Koyanagi, Y. Katoh, B.D. Wirth, *Phys. Rev. B* 95 (2017), 104103.
- [22] T. Koyanagi, M.J. Lance, Y. Katoh, *Scr. Mater.* 125 (2016) 58.
- [23] L.B.B. Aji, J.B. Wallace, L. Shao, S.O. Kucheyev, *Sci. Rep.* 6 (2016) 30931.
- [24] A. Boule, A. Debelle, *Phys. Rev. Lett.* 116 (2016), 245501.
- [25] J.B. Wallace, L.B.B. Aji, L. Shao, S.O. Kucheyev, *Appl. Phys. Lett.* 106 (2015), 202102.
- [26] Y.R. Lin, C.Y. Ho, C.Y. Hsieh, M.T. Chang, S.C. Lo, F.R. Chen, J.J. Kai, *Appl. Phys. Lett.* 104 (2014), 121909.
- [27] Q. Jia, K. Huang, T. You, A. Yi, J. Lin, S. Zhang, M. Zhou, B. Zhang, B. Zhang, W. Yu, X. Ou, X. Wang, *Appl. Phys. Lett.* 112 (2018), 192102.
- [28] M. Bruel, *Electron. Lett.* 31 (1995) 120.
- [29] G.K. Celler, S. Cristoloveanu, *J. Appl. Phys.* 93 (2003) 4955.
- [30] A. Baydin, H. Krzyzanowska, M. Dhanunjaya, S.V.S. Nageswara Rao, J.L. Davidson, L.C. Feldman, N.H. Tolk, *APL Mater* 1 (2016) 036102.
- [31] X. Wang, Y.-W. Zhang, D. Han, Y.-B. Zhao, Z.-Q. Zhao, M. Zhang, *Nucl. Sci. Tech.* 57 (2018) 29.
- [32] K. Huang, Q. Jia, T. You, S. Zhang, J. Lin, R. Zhang, M. Zhou, W. Yu, B. Zhang, X. Ou, X. Wang, *Nucl. Instrum. Meth. B* 406 (2017) 656.
- [33] X. Zhang, Q. Li, M. Wang, Z. Zhang, S. Akhmedaliev, *Nucl. Instrum. Meth. B* 436 (2018) 107.
- [34] J. Woerle, T. Prokscha, A. Hallén, U. Grossner, *Phys. Rev. B* 100 (2019), 115202.
- [35] N. Daghbouj, B.S. Li, M. Callisti, H.S. Sen, J. Lin, X. Ou, M. Karlik, T. Polcar, *Acta Mater.* 188 (2020) 609.
- [36] A. Barcz, R. Jakiela, M. Kozubal, J. Dyczewski, G.K. Celler, *Nucl. Instrum. Meth. B* 365 (2015) 146.
- [37] J.F. Ziegler, J.P. Biersack, U. Littmarck, *The Stopping and Range of Ions in Solids*, Pergamon Press, New York, 1985.
- [38] J. Younes, Z. Harajli, M. Soueidan, D. Fabrègue, Y. Zaatar, M. Kazan, *J. Appl. Phys.* 127 (2020), 173101.
- [39] S. Hamyeh, R. Tauk, P.-M. Adam, M. Kazan, *J. Appl. Phys.* 128 (2020), 095105.
- [40] J. Opsal, A. Rosencwaig, D.L. Willenborg, *Appl. Opt.* 22 (1983) 3169.
- [41] P.K. Kuo, L.D. Favro, R.L. Thomas, *Photothermal Investigation of Solids and Fluids*, in: J.A. Sell, Academic Press, Inc., 1988, Chap. 6, pp. 204-212.
- [42] M. Kazan, *J. Appl. Phys.* 102 (2007), 073532.
- [43] X. Qian, P. Jiang, R. Yang, *Mater. Today Phys.* 3 (2017) 70.
- [44] N.H. Protik, A. Katre, L. Lindsay, J.U. Carrete, N. Mingo, D. Broido, *Mater. Today Phys.* 1 (2017) 31.
- [45] C. Mion, J.F. Muth, E.A. Preble, D. Hanser, *Appl. Phys. Lett.* 89 (2006), 092123.
- [46] P. Carruthers, *Phys. Rev.* 114 (1959) 995.
- [47] Y. Mao, Y. Li, Y. Xiong, W. Xiao, *Comput. Mater. Sci.* 152 (2018) 300.
- [48] M. Khafizov, C. Yablinsky, T.R. Allen, D.H. Hurely, *Nucl. Instrum. Meth. B* 325 (2014) 11.
- [49] J.-P. Crocombette, L. Proville, *Appl. Phys. Lett.* 98 (2011) 191905.
- [50] H. Karakachian, M. Kazan, *J. Appl. Phys.* 121 (2017), 093103.
- [51] P. Perlin, J. Camassel, W. Knap, T. Taliercio, J.C. Chervin, T. Suski, I. Grzegory, S. Porowski, *Appl. Phys. Lett.* 67 (1995) 2524.
- [52] T. Kozawa, T. Kachi, H. Kano, Y. Taga, M. Hashimoto, N. Koide, K. Manabe, *J. Appl. Phys.* 75 (1994) 1098.
- [53] A.S. Barker Jr., M. Ilegems, *Phys. Rev. B* 7 (1973) 743.
- [54] R. Kirste, S. Mohn, M.R. Wagner, J.S. Reparaz, A. Hoffmann, *Appl. Phys. Lett.* 101 (2012) 41909.
- [55] M.V. Balois, N. Hayazawa, A. Tarun, S. Kawata, M. Reiche, O. Moutanabbir, *Nano Lett.* 14 (2014) 3793.